Computational Particle Mechanics
https://doi.org/10.1007/s40571-024-00773-4

Discrete element model for effective electrical conductivity of spark plasma sintered porous materials

F. Nisar[1] · J. Rojek[1] · S. Nosewicz[1] · J. Szczepański[1] · K. Kaszyca[2] · M. Chmielewski[2]

Received: 16 February 2024 / Revised: 24 April 2024 / Accepted: 5 May 2024

Abstract

This paper aims to analyse electrical conduction in partially sintered porous materials using an original resistor network model within discrete element framework. The model is based on sintering geometry, where two particles are connected via neck. Particle-to-particle conductance depends on neck size in sintered materials. Therefore, accurate evaluation of neck size is essential to determine conductance. The neck size was determined using volume preservation criterion. Additionally, grain boundary correction factor was introduced to compensate for any non-physical overlaps between particles, particularly at higher densification. Furthermore, grain boundary resistance was added to account for the porosity within necks. For numerical analysis, the DEM sample was generated using real particle size distribution, ensuring a heterogeneous and realistic microstructure characterized by a maximum-to-minimum particle diameter ratio of 15. The DEM sample was subjected to hot press simulation to obtain geometries with different porosity levels. These representative geometries were used to simulate current flow and determine effective electrical conductivity as a function of porosity. The discrete element model (DEM) was validated using experimentally measured electrical conductivities of porous NiAl samples manufactured using spark plasma sintering (SPS). The numerical results were in close agreement with the experimental results, hence proving the accuracy of the model. The model can be used for microscopic analysis and can also be coupled with sintering models to evaluate effective properties during the sintering process.

Keywords Discrete element method · Effective electrical conductivity · Porous materials · Sintering · Resistor network model

1 Introduction

Spark plasma sintering (SPS) is a powder consolidation method which employs the flow of electric current through graphite tools and powder (if conductive) to generate heat. It is used to manufacture various materials from conductive and non-conductive powders such as transparent ceramics, thermal barrier coatings, thermoelectric and magnetic materials [1, 2], as well as different types of porous materials [3]. Porous materials are usually characterized by effective properties such as effective thermal or electrical conductivity. Electrical properties are especially important for materials manufactured for certain applications, such as electrical contacts [4, 5], solid-state batteries, electrodes, capacitors, magnetic and thermoelectric materials [6–8]. It is also important to investigate effective electrical conductivity during densification of conductive powders. The results can be useful for process design and modelling [9, 10].

Effective electrical properties of porous materials manufactured by SPS have been extensively researched, both

✉ F. Nisar
fnisar@ippt.pan.pl

J. Rojek
jrojek@ippt.pan.pl

S. Nosewicz
snosew@ippt.pan.pl

J. Szczepański
jszczepa@ippt.pan.pl

K. Kaszyca
Kamil.Kaszyca@imif.lukasiewicz.gov.pl

M. Chmielewski
Marcin.Chmielewski@imif.lukasiewicz.gov.pl

[1] Institute of Fundamental Technological Research, Polish Academy of Sciences, Pawińskiego 5B, 02-106 Warsaw, Poland

[2] Lukasiewicz Research Network, Institute of Microelectronics and Photonics, Wólczyńska 133, 01-919 Warsaw, Poland

Published online: 28 May 2024

theoretically and experimentally. Based on experimental results, various analytical approximations of effective electrical conductivity as a function of porosity are proposed and assessed in literature, cf. [4, 11–13]. Because of the thermal–electrical analogy, the relations derived for thermal conductivity are sometimes used for electrical conductivity [4] or combined together to study generalized transport properties [11].

Effective thermal and electrical conductivities of porous materials can be evaluated using analytical models formulated as an extension of micromechanical models originally proposed for composite materials [14]. Similarly, Batchelor and O'Brien [15] derived the effective thermal and electrical conductivity of randomly arranged grains immersed in a matrix, where porous materials can be considered a special case. Many analytical models exploit a relationship between tortuosity and conductivity [13, 16, 17]. Tortuosity, defined as a ratio of effective flow path to straight-line distance in the macroscopic flow direction, is one of the main parameters characterizing porous material. Most of these analytical models are based on simplified models or geometries. More possibilities can be explored numerically. Effective conductivity can be determined using numerical homogenization employing finite element method (FEM) [18–20], finite difference method (FDM) [21] or discrete element method, e.g. [22–24]. The discrete element method (DEM) is an efficient modelling method for sintered porous materials. DEM model consisting of an assembly of particles accurately represents actual microstructure composed of particles connected via necks.

The DEM was first proposed for the dynamics of granular materials but later was successfully applied to thermal and electrical problems. Schneider et al. [25, 26] modelled electrodes of solid oxide fuel cells (SOFC) with monosized sintered particles to calculate their effective conductivity. The same model was used by Roussel et al. [27] who compared the results of the DEM calculations with those performed on the microstructure obtained from micro-CT. Renouf and Fillot [28] investigated electrical characteristics of granular material coupling electrical and mechanical effects in the DEM. Bourbatache et al. [29] studied electrical transfer in metallic granular materials under mechanical loading using an original DEM model with several electrical potentials inside a particle. Zohdi [30] developed a DEM model for electrical current flow within the thermal-electrical–mechanical coupled framework. Hubert et al. [31] proposed an original method to simulate the electrical conduction in continuum with the DEM. Birkholz et al. [18] studied the effective electrical conductivity of granular materials using the DEM model. Effective transport properties in granular lithium-ion battery electrodes were studied by Becker et al. [32] using the DEM with ellipsoidal particles. The DEM was employed by Zhu et al. [33] and Zeng et al. [34] to investigate electrical properties of a shearing powder layer.

The electrical models in all the mentioned works except [29] constitute resistance networks with particle centres as nodes of the electrical circuits. The governing equations were derived from first Kirchhoff's law. The branches connecting nodes represent the inherent resistance of particles and additional contact resistance in unbonded granular material or grain boundary resistance in bonded granular material. In sintered materials, particles are connected by the neck, and the grain boundary resistance is determined by the neck size and porosity in the necks. Therefore neck size evaluation is important to study conduction between particles. Neck size in DEM sintering models is commonly calculated according to Coble's sintering model [35]. It gives a good estimation of neck size in the initial stages of sintering, but it is shown to overestimate neck size for higher densification [36].

An original model of two-particle sintering geometry, where the neck size was determined based on the volume conservation principle, was proposed by Rojek et al. [36]. This geometry was used to obtain analytical relation between thermal conductance and neck size. Considering the analogy between thermal and electrical problems, the model proposed in [36] can also be used for electrical conduction of sintered materials.

This work aims to model electrical conduction in partially sintered porous materials using the DEM model presented in [36]. The model was originally developed for heat conduction and was used to study effective thermal conductivity in sintered porous materials [37]. The thermal model was implemented for transient heat transfer analysis with the heat conduction equations integrated in time using the explicit forward Euler method. In the electrical problem, transient response is very short, and it can be neglected in most cases. Electrical current flow in a resistance network is considered a steady-state problem, described by the system of linear algebraic equations. The system of linear algebraic equations in the DEM algorithms for electrical problems is often solved using iterative methods, cf. [28, 31, 34]. In this work, the electrical problem will implemented in the framework for a transient solution. It will be shown that the recursive formula obtained in the forward Euler method is identical to that in a general iterative scheme, the subsequent solutions are actual approximations from the iterative scheme, and the convergence criterion is equivalent to the stability criterion of the time integration scheme.

The model is applied to simulate electric current flow in partially sintered NiAl samples with different porosity levels. DEM samples are obtained from sintering simulation of NiAl, which is performed on the sample generated using real particle size distribution. Hence the heterogeneity of the samples is quite high with a maximum to minimum particle size ratio of 15. The DEM model employing constant volume

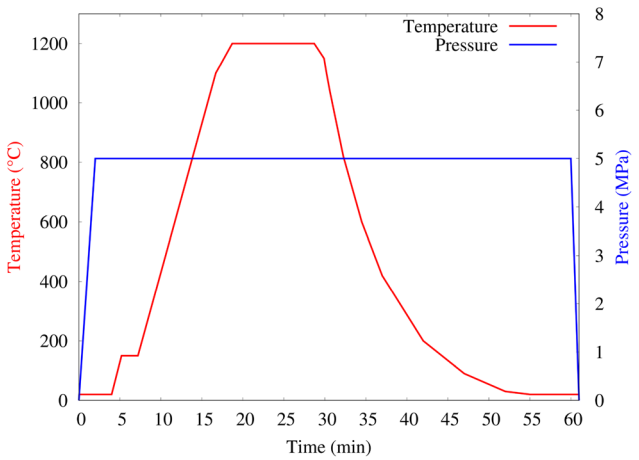

Fig. 1 Temperature and pressure profiles for the whole sintering cycle of sample 1 (as an example)

criterion for the calculation of neck size is further improved by adding a correction factor to make up for the non-physical overlaps. Moreover, additional resistance at the interface or grain boundary is added to account for the porosity in the necks. This makes the model applicable over a broad range of densities. The electrical properties of NiAl with different porosities are investigated experimentally, and the data are used for model validation. The present study is also important for process designing, as it can be used to determine potential evolution during the sintering process, where the sample is continuously undergoing densification.

2 Manufacturing of porous samples

DEM model for conduction was validated using experimental measurements on porous intermetallic NiAl samples manufactured using SPS. NiAl powder (Goodfellow, 99.9% pure) was sintered using different processing parameters to obtain cylindrical samples with varying porosity, as presented in Table 1. Fig. 1 illustrates temperature and pressure profiles for the sintering cycle of sample 1. SPS sintering process begins with applying pressure, followed by heating. At first, the sample is heated to 150 °C and held there for 2 min to stabilize the heating. Then, the sample is heated to 1100 °C at a rate of 100 K/min. After that, the heating rate is decreased to 50 K/min to prevent overheating. Once reaching the maximum sintering temperature of 1200 °C, the sample is held for 10 min to allow enough time for sintering. Then the sample is allowed to cool down to room temperature uncontrollably. Finally, the pressure is released and the sample is retrieved.

Density ρ of these samples was measured using Archimedes principle, and porosity was calculated as: $1-(\rho/\rho_0)$, where theoretical bulk density $\rho_0 = 5.90\,\mathrm{g/cm^3}$. Microscopic analysis of these samples was performed using SEM (Hitachi S4100) to study sintering mechanism. Figure 2 shows an SEM image of the sample with 0.164 porosity, where connections between particles in the form of necks can be seen. During sintering, necks form between particles and grow due to mass transport, resulting in pore reduction. Figure 2 shows fractured necks, where a significant amount of porosity can be seen. This finding is particularly significant as the porosity present in necks provides additional resistance, thus reducing conductance.

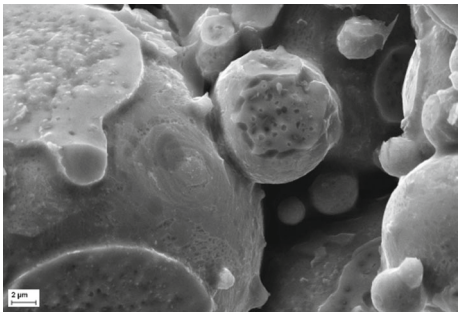

Fig. 2 SEM images showing porosity in necks, sample with 0.164 porosity

The electrical resistance of these sintered samples was measured using four-point probe method, which was then converted to electrical conductivity κ. Conductivity with respect to porosity is presented in Table 1.

3 Formulation of the discrete element method

3.1 Governing equations for conduction

The discrete element method for electrical conduction considers an assembly of contacting particles where the centres represent circuit nodes connected via resistors, as shown in Fig. 3. The formulation follows first Kirchhoff's law, which states that the sum of current entering and leaving a node is zero, so for the i-th particle we have:

$$I_i = \sum_{i=1}^{n_i^c} I_{ij} = 0, \tag{1}$$

where I_i is the resultant current for the i-th particle, I_{ij} is current through the branch connecting nodes i and j, and n_i^c is the number of particles in contact with the i-th particle. I_i may also include an externally supplied source I_i^{ext},

$$I_i = \sum_{j=1}^{n_c} I_{ij} - I_i^{\mathrm{ext}} = 0. \tag{2}$$

Table 1 SPS sintering processing parameters and density

	Heating rate (K/min)	Sintering temperature (°C)	Pressure (MPa)	Holding time (min)	Porosity	Electrical conductivity κ (S/m)
Sample 1	100	1200	5	10	0.216	4.33×10^5
Sample 2	100	1300	5	10	0.164	6.14×10^5
Sample 3	100	1100	30	10	0.106	7.44×10^5
Sample 4	100	1200	30	10	0.050	8.77×10^5

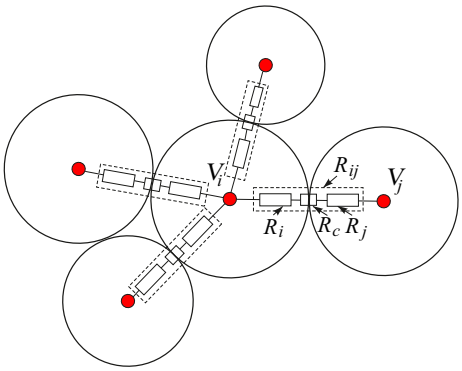

Fig. 3 Resistance network model—circuit using centres as nodes connected via resistor branches

The current between connected particles I_{ij} is given by the Ohm's law

$$I_{ij} = \frac{V_j - V_i}{R_{ij}} = K_{ij}(V_j - V_i), \tag{3}$$

where V_i and V_j are particle voltages, and R_{ij} and K_{ij} are the resistance and conductance between two nodes, respectively.

The first Kirchhoff's law can be written in a global matrix form (for all the nodes):

$$\mathbf{KV} = \mathbf{I} \tag{4}$$

where vector $\mathbf{V}$ contains all the nodal voltages $\mathbf{V} = \{V_1, V_2, \ldots, V_N\}^{\mathrm{T}}$, N is the number of particles, vector $\mathbf{I}$ contains either zeros or external currents $\mathbf{I} = \{0, 0, \ldots, I_i^{\mathrm{ext}}, \ldots, 0\}^{\mathrm{T}}$, and the global conductance matrix $\mathbf{K}$ is assembled from the conductances of all the branches in the network K_{ij}. If there are no external currents Eq. (4) takes the form:

$$\mathbf{KV} = \mathbf{0} \tag{5}$$

The form of Eq. (4) is the same as that of FEM equation for static equilibrium, and the conductance matrix $\mathbf{K}$ is analogous to the stiffness matrix. Similar to the stiffness matrix for non-restricted system, the conductance matrix $\mathbf{K}$ is singular, and the system of equations (4) or (5) cannot be solved. To solve these equations, it is necessary to prescribe voltage to at least one node.

Let us assume that vector $\mathbf{V}_{\mathrm{p}}$ contains the prescribed nodal voltages and $\mathbf{V}_{\mathrm{u}}$ contains unprescribed (free) nodal voltages. Accordingly, vector $\mathbf{V}$ can be decomposed as follows:

$$\mathbf{V} = \begin{Bmatrix} \mathbf{V}_{\mathrm{u}} \\ \mathbf{V}_{\mathrm{p}} \end{Bmatrix} \tag{6}$$

Hence, Eq. (4) can be decomposed as follows:

$$\begin{bmatrix} \mathbf{K}_{\mathrm{uu}} & \mathbf{K}_{\mathrm{up}} \\ \mathbf{K}_{\mathrm{up}}^{\mathrm{T}} & \mathbf{K}_{\mathrm{pp}} \end{bmatrix} \begin{Bmatrix} \mathbf{V}_{\mathrm{u}} \\ \mathbf{V}_{\mathrm{p}} \end{Bmatrix} = \begin{Bmatrix} \mathbf{I}_{\mathrm{u}} \\ \mathbf{I}_{\mathrm{p}} \end{Bmatrix} \tag{7}$$

Remark: voltage and current cannot be prescribes simultaneously to the same node. The unknown nodal voltages can be determined by solving the following equation:

$$\mathbf{K}_{\mathrm{uu}}\mathbf{V}_{\mathrm{u}} = \mathbf{I}_{\mathrm{res}} \tag{8}$$

where

$$\mathbf{I}_{\mathrm{res}} = \mathbf{I}_{\mathrm{u}} - \mathbf{K}_{\mathrm{up}}\mathbf{V}_{\mathrm{p}}. \tag{9}$$

3.2 Solution algorithm

Equation (8) can be solved using any method of solving a system of linear equations. We adopt here an iterative solution derived as follows using the framework of the explicit time integration of the transient state analysis. For algorithmic reasons, let us introduce an additional term to Eq. (8)

$$\mathbf{C}_{\mathrm{uu}}\dot{\mathbf{V}}_{\mathrm{u}} + \mathbf{K}_{\mathrm{uu}}\mathbf{V}_{\mathrm{u}} = \mathbf{I}_{\mathrm{res}} \tag{10}$$

Analogously to the heat capacitance the capacitance matrix $\mathbf{C}_{\mathrm{uu}}$ it will be taken in the diagonal form with particle capacitance assumed as

$$C_i = m_i c_i, \tag{11}$$

where m_i—particle mass, c_i—specific capacity used for numerical purposes. To integrate the system of the first-order ODE given by Eq. (10), we use the forward Euler explicit scheme:

$$\mathbf{C}_{\mathrm{uu}}\frac{\mathbf{V}_{\mathrm{u}}^{i+1} - \mathbf{V}_{\mathrm{u}}^{i}}{\Delta t} = \mathbf{I}_{\mathrm{res}} - \mathbf{K}_{\mathrm{uu}}\mathbf{V}_{\mathrm{u}}^{i} \tag{12}$$

The solution for time t^{n+1} can be obtained as follows:

$$\mathbf{V}_{\mathrm{u}}^{i+1} = \left(\mathcal{I} - \Delta t \mathbf{C}_{\mathrm{uu}}^{-1}\mathbf{K}_{\mathrm{uu}}\right)\mathbf{V}_{\mathrm{u}}^{i} + \Delta t \mathbf{C}_{\mathrm{uu}}^{-1}\mathbf{I}_{\mathrm{res}} \tag{13}$$

where $\mathcal{I}$ is the identity matrix. The form of Eq. (13) is identical to the general form of equation used for the iterative solution of the linear equations cf. [38]. The diagonal matrix $\mathbf{C}_{\mathrm{uu}}$ ensures efficiency of the solution for a single iteration since its inverse is trivial. Starting from a certain initial vector of nodal voltages $\mathbf{V}_{\mathrm{u}}^{0}$ the iterative procedure gives a sequence of vectors $\mathbf{V}_{\mathrm{u}}^{i}$ converging to the solution $\mathbf{V}_{\mathrm{u}}$ of Eq. (8). The convergence is monitored using the convergence indicator $g_{\max}^{i+1}$ defined as maximum relative change of voltage at iteration $i+1$ taken over all particles n ($1 \le n \le N$):

$$g_{\max}^{i+1} = \max_{1\le n\le N}\left|\frac{V_n^{i+1} - V_n^{i}}{V_n^{i+1}}\right| \tag{14}$$

$g_{\max}^{i+1}$ The convergence is assumed when the convergence indicator is below a certain tolerance β:

$$g_{\max}^{i+1} \le \beta \tag{15}$$

Back substitution of evaluated voltages $\mathbf{V}_{\mathrm{u}}$ into the second block equation (7) yields currents for the imposed potentials $\mathbf{I}_{\mathrm{p}}$:

$$\mathbf{I}_{\mathrm{p}} = \mathbf{K}_{\mathrm{up}}^{\mathrm{T}}\mathbf{V}_{\mathrm{u}} + \mathbf{K}_{\mathrm{pp}}\mathbf{V}_{\mathrm{p}} \tag{16}$$

It is shown in the Appendix that the convergence criterion of the iterative procedure defined by Eq. (13) is identical to the stability criterion of the forward Euler scheme.

3.3 Equivalent conductance

In the resistance network model (Fig. 3), effective resistance R_{ij} of the branch connecting two nodes is the sum of all resistors in series, such that

$$R_{ij} = R_i + R_j + R_c, \tag{17}$$

where resistors R_i and R_j represents resistance of particles i and j, while R_c is the contact resistance. Conductance K is the inverse of resistance R. Therefore, Eq. (17) can be written as:

$$K_{ij} = \frac{K_i K_j K_c}{K_i K_j + K_j K_c + K_i K_c}. \tag{18}$$

Electrical conductance of a hemisphere K_i or K_j can be evaluated using the same geometry and model developed for the thermal problem in [36]. The equivalent conductance K_i is normalized by the conductance K_{cyl}^{i} of the cylinder of

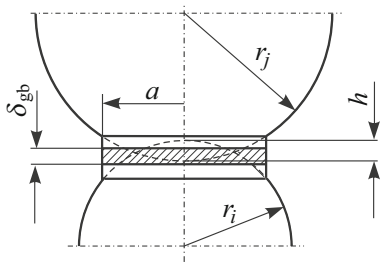

Fig. 4 Two particles of different sizes connected by the neck

radius and height r_i, enclosing the hemisphere, and a linear relation between neck size a and conductance K_i was obtained:

$$\frac{K_i}{K_{\mathrm{cyl}}^{i}} = 1.08\frac{a}{r_i}, \tag{19}$$

where

$$K_{\mathrm{cyl}}^{i} = \lambda\frac{\pi r_i^2}{r_i} = \lambda\pi r_i, \tag{20}$$

where thermal conductivity λ can be replaced with electrical conductivity κ.

For neck size a calculation, generally Coble's sintering model [35] is used e.g. [39–42]:

$$a = \sqrt{2r^{*}h}, \tag{21}$$

where $r^{*} = 2r_i r_j/(r_i + r_j)$ is the effective radius, and h is the overlap. However, it is shown in [36] that Coble's model overestimates neck size, especially for increasingly large overlaps at higher densification.

Therefore, in this work, we will use a more appropriate two-particle sintering geometry proposed in [36], as shown in Fig. 4. It is assumed that the volume of overlap is redistributed to the cylindrical neck, and the neck radius is calculated based on volume conservation criterion.

3.4 Correction of neck size for higher density

For the validation of the DEM electrical model, we generated geometries with different porosity levels using sintering simulation with the model formulated in [43]. This model considers the interaction between two interacting particles, but it neglects the possible interaction with other particles in contact. This may lead to non-physical neck overlaps when particles have multiple contacts. These non-physical overlaps can be tracked using

grain boundary fraction [44], which is defined for each particle as the ratio of the sum of necks and particle surfaces:

$$f_i^{gbf} = \frac{\sum_{j=1}^{n_c} S_{ij}^{\text{neck}}}{S_i}, \tag{22}$$

The grain boundary fraction cannot be greater than 1

$$f_i^{gbf} \leq 1. \tag{23}$$

If the condition in Eq. (23) is not fulfilled, all the necks of the i-th particle are reduced using a scaling factor α_i

$$a_{ij}^{\text{corr}} = \alpha_i a_{ij}. \tag{24}$$

By substituting (24) into (22) from inequality (23) we obtain

$$\alpha_i \leq \frac{2r_i}{\sqrt{\sum_{j=1}^{n_c} (a_{ij})^2}}. \tag{25}$$

3.5 Conductance of the neck

SEM analysis of fractured surface (Sec. 2) revealed a significant amount of porosity in the necks, as shown in Fig. 2. These pores provide additional resistance at the grain boundary within necks. This additional resistance must be considered in the model. For this, we approximately assume a layer of grain boundary thickness δ_{gb} based on microscopic analysis of grain boundaries of sintered samples (Fig. 5). In this layer, bulk conductivity κ is reduced by a conductivity reduction factor ε ($0 < \varepsilon < 1$), such that $\kappa_{\text{gb}} = \varepsilon\kappa$. The conductance K_c of cylindrical neck with radius a and height δ_{gb} (Fig. 4) can be calculated as follows:

$$K_c = \frac{\varepsilon\kappa\pi a^2}{\delta_{\text{gb}}}. \tag{26}$$

Grain boundary thickness δ_{gb} and conductivity reduction factor ϵ are considered to be fitting parameters in model calibration.

4 Results

The presented DEM model is used to simulate conduction in cylindrical samples representing partially sintered NiAl material with different porosity levels. The DEM samples were obtained by thermo-mechanical simulation of pressure assisted sintering also known as hot pressing. The representative geometries with varying porosity levels were retrieved from hot press simulation and were subjected to electrical simulation using the model presented herein. The effective conductivities were evaluated and compared to experimental results. The electrical analysis consisted of two stages. First, the model without additional grain boundary resistance was used. In the second stage, the full model with grain boundary resistance was employed. The fitting parameters, grain boundary thickness and conductivity reduction factor were calibrated on one of the samples, and then the model with calibrated parameters was validated on the other three samples. Both calibration and validation procedures were based on comparison of numerical effective electrical conductivity with experimental measurements presented in Sec. 2.

4.1 DEM sample generation and characterization

The DEM model of over 17,000 particles was generated for hot pressing simulation using real particle size distribution with a diameter ranging from 1.5 to 20 µm. Loose particles, randomly distributed in space and confined in a cylinder, were allowed to fall under gravitational force while cylindrical walls contracted resulting in an initial or tap density of 65%. The cylindrical DEM sample had a diameter and height of 123.6 µm and 202 µm, respectively. Then, the DEM sample was used to simulate hot pressing using the thermo-viscoelastic model presented in [43]. The material parameters essential for sintering simulation (i.e. dihedral angle, surface energy, theoretical density, coefficient of thermal expansion, enthalpy for diffusion, etc) were the same as presented in [43]. The sintering simulation was paused at various intervals to obtain representative DEM samples with porosities similar to experimentally manufactured NiAl samples.

The DEM method allows us to track the neck size growth. This enables a more comprehensive understanding of current flow since neck size, as discussed earlier, is a predominant factor affecting conduction in sintered materials. Figure 6 shows neck size distribution in DEM samples with different porosities, where neck size is normalized by the minimum radius of the two contacting particles:

$$r_{\text{min}} = \min(r_i, r_j) \tag{27}$$

The right shift observed in the histograms of neck size distribution with decreasing porosity indicates neck growth during sintering. The observations were consistent with the sintering theory and the real process.

4.2 Conduction simulation

Electrical conduction in partially sintered samples was simulated using the theoretical density ρ_0 of 5910 kg m^{-3} and electrical conductivity κ_e of 9.8×10^5 S m^{-1}, while the specific capacity c of 2×10^6 F kg^{-1} was used as a numerical parameter. Current flow in the axial direction was produced by fixing 3.5×10^{-5} V at the top layer of particles and 0 V at the bottom and assuming insulation at the cylindrical sur-

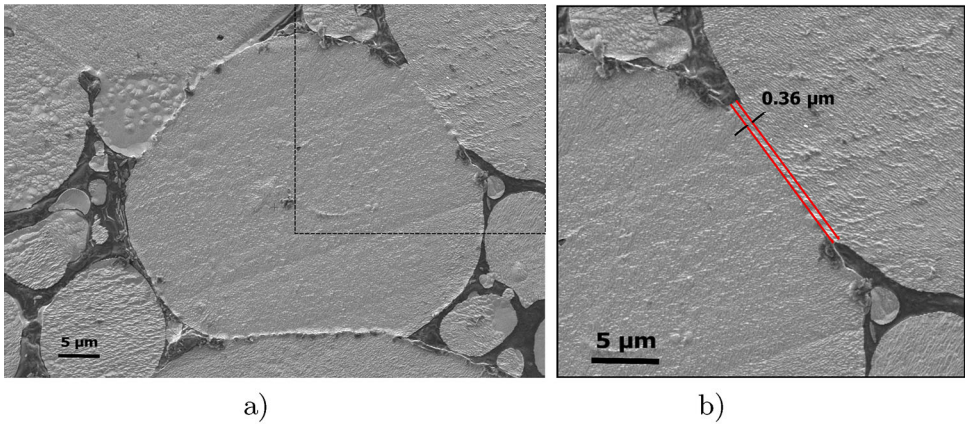

Fig. 5 SEM image showing grain boundaries in sintered NiAl sample with porosity 0.05 **a** multiple grain boundaries visible, **b** zoomed image of one boundary with a measured thickness of 0.36 µm

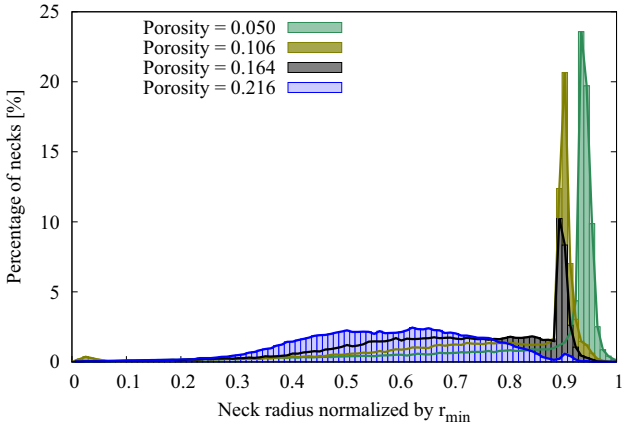

Fig. 6 Neck size distribution w.r.t porosity

face. The convergence tolerance β as described in Eq. (15) was set to be 0.0002. The evolution of electrical potential and its convergence is presented in Fig. 7 for one of the samples with porosity 0.164. Figure 7a shows the convergence indicator as a function of number of iterations. Figure 7b shows the increase in potential in different particles at different heights in the samples. The solution reached convergence tolerance limit after 40 iterations with a time-step of 5 µs, which was calculated using Eq. (43). The final solution is shown in Fig. 7c. It is characterized by linear variation of the potential along the sample height.

4.3 Effective conductivity

The solutions for all four DEM samples with different porosities were used to calculate effective electrical conductivity κ_{eff} employing Ohm's law on the cylindrical geometry:

$$\kappa_{\text{eff}} = -\frac{IL}{\Delta V A}, \tag{28}$$

where I is the total current through the cross-sectional area A of the sample, ΔV is the potential difference between the top and bottom of the sample with height L. The total current I was calculated by summing currents from particles with prescribed potential at the top or bottom of the sample

$$I_{\text{top}} = \sum_{i=1}^{n_{\text{top}}} I_i, \tag{29}$$

$$I_{\text{bottom}} = \sum_{i=1}^{n_{\text{bottom}}} I_i, \tag{30}$$

where n_{top} and n_{bottom} are number of particles with prescribed voltage at the top and bottom of the sample, respectively. The total current through the top, bottom, and all other cross sections are equal.

$$I = I_{\text{top}} = I_{\text{bottom}}. \tag{31}$$

The numerical results from the DEM model without grain boundary resistance are shown in Fig. 8. The numerical results are compared with experimental results. A clear trend can be observed, suggesting an inverse relation between porosity and conductivity. Numerical results without grain boundary resistance, though close, still show noticeable deviation from the experimental results, hence demonstrating the need to consider porosity at the grain boundary. Similar observations were also presented in [20], where the effective thermal conductivity was evaluated using FEM.

Additional grain boundary resistance was added to the model, as given in Eq. (26). The equation includes two parameters, grain boundary thickness δ_{gb} and conductivity reduction factor ϵ, that require calibration. For calibration, a parametric study was performed on the sample with a porosity of 0.164. The range of grain boundary thickness (0.1–0.3 µm) in the parametric study overlapped the range obtained from microscopic SEM analysis (0.15–0.4 µm), presented in Fig. 5. In this parametric study, conductivity in the grain boundary layer was reduced using conductivity reduction factor ϵ in the range of 0.1–0.5.

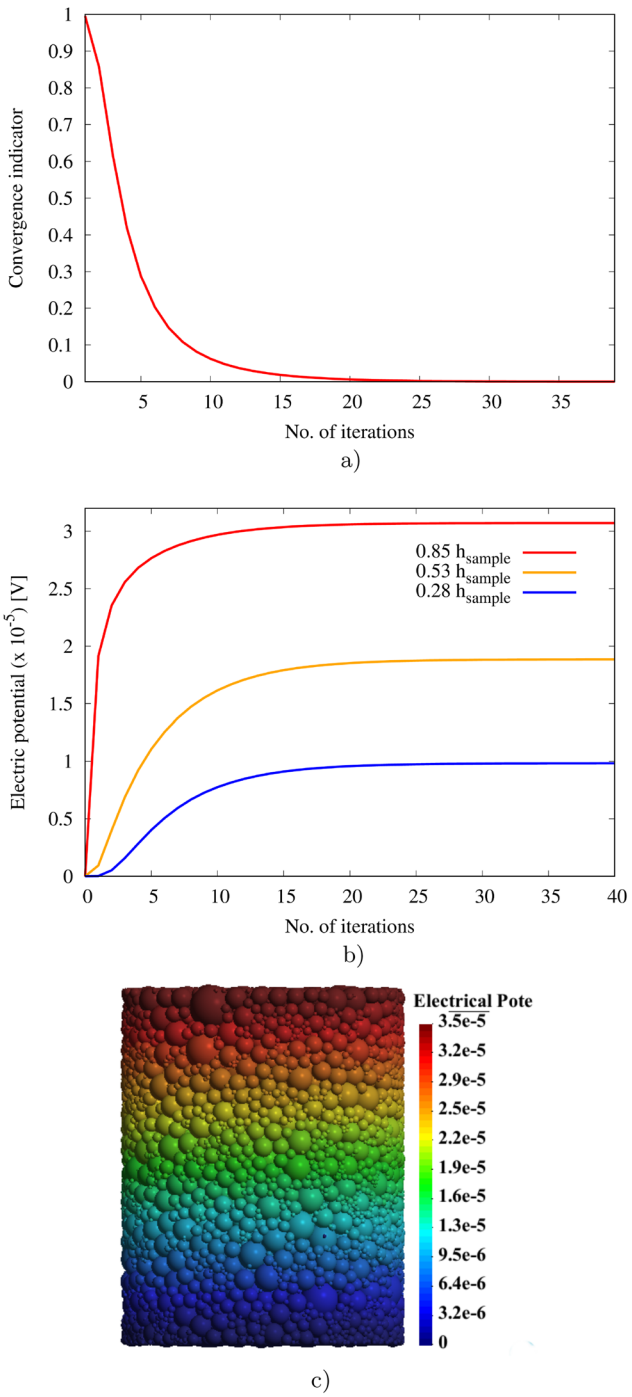

Fig. 7 Solution for the sample with porosity of 0.164: **a** convergence indicator, **b** converging solution at different heights across the sample, **c** final potential distribution across the sample

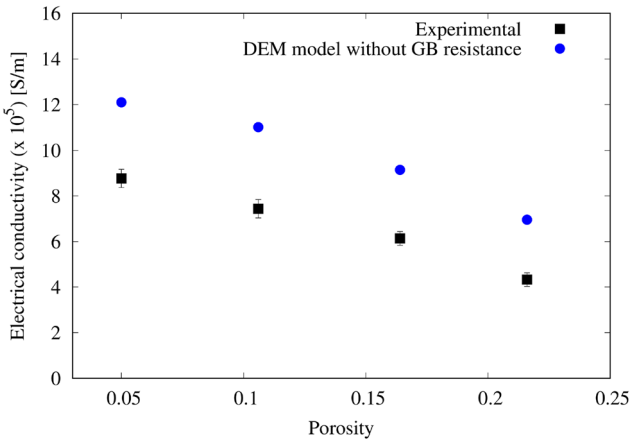

Fig. 8 Effective conductivity without grain boundary resistance as a function of porosity

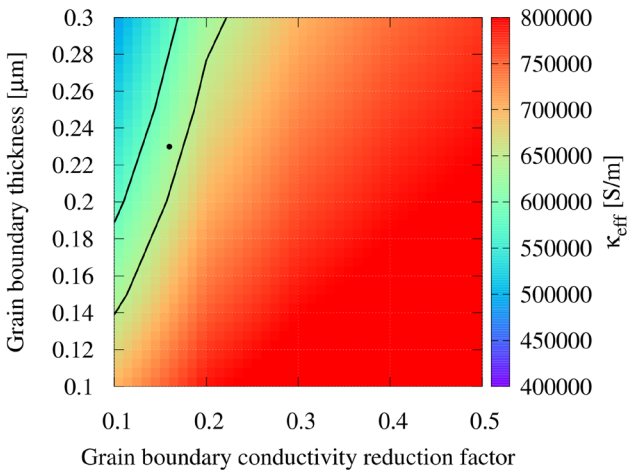

Fig. 9 Map representing parametric study to calibrate grain boundary thickness and conductivity reduction factor

Electrical conductivities obtained for different combinations of δ_{gb} and ϵ are represented in form of a map in Fig. 9. The lines confine experimental conductivity with error. Any combination of δ_{gb} and ϵ can be used to obtain valid conductivity results from the numerical model. However, for further analysis, the values of ε and δ_{gb} were taken as 0.16 and 0.23 µm, respectively.

These values of the parameters were used to validate the model on the other three samples. The effective conductivities with the additional grain boundary resistance for all the samples are shown in Fig. 10. These numerical results are compared with the experimental results. It can be observed that numerical results with additional grain boundary resistance are in close proximity to the experimental measurements. This demonstrates the validity of the DEM model over the given range of porosity.

5 Conclusions

An original DEM electrical model was formulated by exploiting the analogy between thermal and electrical problems. Heat conduction model based on thermal pipe network, pro-

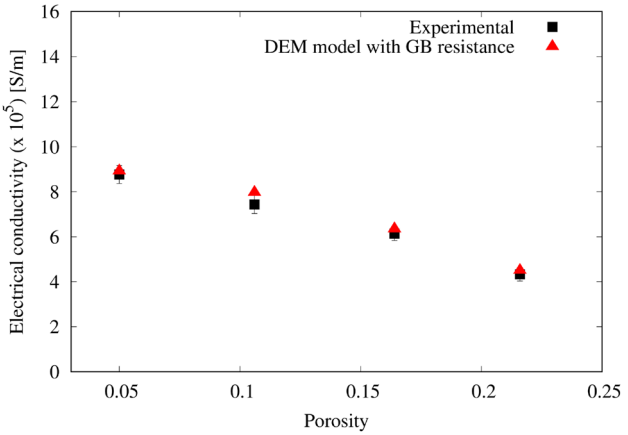

Fig. 10 Effective conductivity as a function of porosity with additional grain boundary resistance

posed in [36], was used to develop resistor network model for electrical problems. The model was implemented in the framework for transient analysis. The set of linear algebraic equations for the electrical problem were solved iteratively. It was shown that the expression obtained from explicit forward Euler approach was identical to that obtained from iterative method.

The model was validated using experimental measurements on NiAl samples with varying porosity levels fabricated using SPS. Experimental investigation demonstrated the decrease in conductivity with increasing porosity. SEM analysis of fractured surfaces revealed a significant amount of porosity in the necks, even for higher densifications. These findings were used to enhance the model by introducing grain boundary resistance.

The validity of the DEM model was demonstrated on a heterogeneous microstructure generated using real particle size distribution. Microstructural analysis of DEM samples indicated an increase in neck size with decreasing porosity, which was consistent with the sintering theory and the real process.

The electrical conductivity obtained by the DEM model with particle resistance only was largely in agreement with experimental measurements. However, a consistent difference persisted between the predicted and experimental results. This underscored the importance of resistance provided by porosity in the necks, as shown in the SEM analysis. After introducing additional resistance, numerical results were in alignment with the experimental measurements, hence suggesting the validity of the DEM model.

Appendix: Convergence of the iterative solution

Starting from a certain initial vector $\mathbf{V}_{\mathrm{u}}^0$ the iterative procedure defined by Eq. (12) produces a sequence of vectors $\{\mathbf{V}_{\mathrm{u}}^i\}_{i=0,1,2,\ldots}$. The iterative procedure is convergent if for any initial vector $\mathbf{V}_{\mathrm{u}}^0$ the sequence $\{\mathbf{V}_{\mathrm{u}}^i\}_{i=0,1,2,\ldots}$ converges to the exact solution $\mathbf{V}_{\mathrm{u}}$ of Eq. (8). The exact solution should also satisfy the following equation

$$\mathbf{V}_{\mathrm{u}} = \left(\mathbf{I} - \Delta t \mathbf{C}_{\mathrm{uu}}^{-1}\mathbf{K}_{\mathrm{uu}}\right)\mathbf{V}_{\mathrm{u}} + \Delta t \mathbf{C}_{\mathrm{uu}}^{-1}\mathbf{I}_{\mathrm{res}} \tag{32}$$

Subtracting Eq. (32) from Eq. (12) we obtain the recurrence formula

$$\mathbf{V}_{\mathrm{u}}^{i+1} - \mathbf{V}_{\mathrm{u}} = \left(\mathbf{I} - \Delta t \mathbf{C}_{\mathrm{uu}}^{-1}\mathbf{K}_{\mathrm{uu}}\right)\left(\mathbf{V}_{\mathrm{u}}^{i} - \mathbf{V}_{\mathrm{u}}\right) \tag{33}$$

By repeating this step, we obtain:

$$\mathbf{V}_{\mathrm{u}}^{i+1} - \mathbf{V}_{\mathrm{u}} = \left(\mathbf{I} - \Delta t \mathbf{C}_{\mathrm{uu}}^{-1}\mathbf{K}_{\mathrm{uu}}\right)^{i}\left(\mathbf{V}_{\mathrm{u}}^{0} - \mathbf{V}_{\mathrm{u}}\right) \tag{34}$$

The convergence theorem, cf. [45], states that if for some subordinate matrix norm $\|\cdot\|$

$$\left\|\mathbf{I} - \Delta t \mathbf{C}_{\mathrm{uu}}^{-1}\mathbf{K}_{\mathrm{uu}}\right\| < 1, \tag{35}$$

the iterative procedure defined by Eq. (33) is convergent, that is:

$$\lim_{i\to\infty}\left\|\mathbf{V}_{\mathrm{u}}^{i} - \mathbf{V}_{\mathrm{u}}\right\| = 0 \tag{36}$$

for any initial vector $\mathbf{V}_{\mathrm{u}}^0$.

Determination of the convergence will be illustrated for a simple system of two particles i and j with the interparticle conductance K_{ij}. Equation (5) for these particles takes the form:

$$\begin{bmatrix} K_{ij} & -K_{ij} \\ -K_{ij} & K_{ij} \end{bmatrix}\begin{Bmatrix} V_i \\ V_j \end{Bmatrix} = \begin{Bmatrix} 0 \\ 0 \end{Bmatrix} \tag{37}$$

The system of linear equations is indefinite. Let us prescribe a certain value of V_j. Then Eq. (37 is reduced to

$$K_{ij}V_i = K_{ij}V_j \tag{38}$$

which corresponds to Eq. (8). By adding the term with the interparticle capacitance C_{ij}, we obtain equation corresponding to Eq. (10)

$$C_{ij}\dot{V}_i + K_{ij}V_i = K_{ij}V_j \tag{39}$$

The iterative solution for V_i can be obtained as follows:

$$V_i^{k+1} = \left(1 - \frac{\Delta t}{C_{ij}} K_{ij}\right) V_i^k + \frac{\Delta t}{C_{ij}} K_{ij} V_j \tag{40}$$

Taking the absolute value as the norm in one-dimensional vector space, the convergence criterion for (40) is given by

$$\left|1 - \frac{\Delta t}{C_{ij}} K_{ij}\right| < 1, \tag{41}$$

which yields the condition

$$\frac{\Delta t}{C_{ij}} K_{ij} < 2. \tag{42}$$

Inequality (42) specifies permissible Δt for given values of C_{ij} and K_{ij} to have convergent solution.

$$\Delta t < \frac{2C_{ij}}{K_{ij}}. \tag{43}$$

Condition (43) is identical to the stability criterion for the forward Euler integration scheme of Eq. (39)

Acknowledgements The authors acknowledge the financial support of the National Science Centre, Poland, within research Project No. 2019/35/B/ST8/03158.

Declarations

Conflict of interest The authors have no relevant financial or non-financial interests to disclose. On behalf of all authors, the corresponding author states that there is no Conflict of interest.

References

1. Guillon O, Gonzalez-Julian J, Dargatz B et al (2014) Field-assisted sintering technology/spark plasma sintering: mechanisms, materials, and technology developments. Adv Eng Mater 16:830–849
2. Bram M, Laptev A, Mishra T et al (2020) Application of electric current-assisted sintering techniques for the processing of advanced materials. Adv Eng Mater 22:2000051. https://doi.org/10.1002/adem.202000051
3. Dudina D, Bokhonov B, Olevsky E (2019) Fabrication of porous materials by spark plasma sintering: a review. Materials 12:541. https://doi.org/10.3390/ma12030541
4. Amalu N, Okorie B, Ugwuoke J et al (2021) Electrical conductivity of spark plasma sintered W-Cu and Mo-Cu composites for electrical contact applications. J Miner Mater Charact Eng 9:48–60. https://doi.org/10.4236/jmmce.2021.91004
5. Weißenfels C, Wriggers P (2010) Numerical modeling of electrical contacts. Comput Mech 46:301–314
6. He P, Wu Y (2021) Constructing of highly porous thermoelectric structures with improved thermoelectric performance. Nano Res 14(10):3608–3615
7. Gucci F (2018) Current assisted sintering of thermoelectric materials. PhD thesis, School of Engineering and Materials Science, Queen Mary, University of London, London
8. Goldsmid H (2009) Porous thermoelectric materials. Materials 2(3):903–910. https://doi.org/10.3390/ma2030903
9. Vanmeensel K, Huang S, Laptev A et al (2009) Modeling of field assisted sintering technology (FAST) and its application to electro-conductive systems. Ceram Eng Sci Proc 29(9):109–122
10. Räthel J, Herrmann M, Beckert W (2009) Temperature distribution for electrically conductive and non-conductive materials during Field Assisted Sintering (FAST). J Eur Ceram Soc 20:1419–1425
11. Aivazov M, Domashnev I (1968) Influence of porosity on the conductivity of hot-pressed titanium-nitride specimens. Sov Powder Metall Met Ceram 7:708–710. https://doi.org/10.1007/BF00773737
12. Sevostianov I, Mogilevskaya S, Kushch V (2019) Maxwell's methodology of estimating effective properties: Alive and wells. Int J Eng Sci 140:35–88
13. Montes J, Cuevas F, Cintas J (2008) Porosity effect on the electrical conductivity of sintered powder compacts. Appl Phys A 92:375–380. https://doi.org/10.1007/s00339-008-4534-y
14. Nikolopoulos P, Ondracek G (1983) Field-property bounds for porous sintered ceramies. J Am Ceram Soc 66:238–241. https://doi.org/10.1111/j.1151-2916.1983.tb15705.x
15. Batchelor G, O'Brien R (1977) Thermal or electrical conduction through a granular material. Proc R Soc Lond A 355:313–333. https://doi.org/10.1098/rspa.1977.0100
16. Yang C, Nakayama A (2010) A synthesis of tortuosity and dispersion in effective thermal conductivity of porous media. Int J Heat Mass Transf 53:3222–3230. https://doi.org/10.1016/j.ijheatmasstransfer.2010.03.004
17. Xu W, Jia M, Gong Z (2018) Thermal conductivity and tortuosity of porous composites considering percolation of porous network: From spherical to polyhedral pores. Compos Sci Technol 167:134–140. https://doi.org/10.1016/j.compscitech.2018.07.038
18. Birkholz O, Gan Y, Kamlah M (2019) Modeling the effective conductivity of the solid and the pore phase in granular materials using resistor networks. Powder Technol 351:54–65
19. Bakker K (1997) Using the finite element method to compute the influence of complex porosity and inclusion structures on the thermal and electrical conductivity. Int J Heat Mass Transf 40:3503–3511
20. Nosewicz S, Jurczak G, Wejrzanowski T et al (2022) Thermal conductivity analysis of porous NiAl materials manufactured by spark plasma sintering: experimental studies and modelling. Int J Heat Mass Transf 194:123070. https://doi.org/10.1016/j.ijheatmasstransfer.2022.123070
21. Xiong Z (2022) Computational homogenization of heterogeneous materials' thermal conductivity by the finite difference method. PhD thesis, Universite Paris-Saclay, Evry, France
22. Moscardini M, Gan Y, Pupeschi S et al (2018) Discrete element method for effective thermal conductivity of packed pebbles accounting for the smoluchowski effect. Fusion Eng Des 127:192–201. https://doi.org/10.1016/j.fusengdes.2018.01.013

23. Haddad H, Leclerc W, Hassan GA et al (2021) Numerical investigation of heat conduction in heterogeneous media with a discrete element method approach. Int J Therm Sci 164:106799. https://doi.org/10.1016/j.ijthermalsci.2020.106799
24. Kiani-Oshtorjani M, Jalali P (2019) Thermal discrete element method for transient heat conduction in granular packing under compressive forces. Int J Heat Mass Transf 145:118753. https://doi.org/10.1016/j.ijheatmasstransfer.2019.118753
25. Schneider LC, Martin CL, Bultel Y et al (2007) Percolation effects in functionally graded sofc electrodes. Electrochim Acta 52:3190–3198. https://doi.org/10.1016/j.electacta.2006.09.071
26. Schneider L, Martin C, Bultel Y et al (2006) Discrete modelling of the electrochemical performance of SOFC electrodes. Electrochim Acta 52:314–324
27. Roussel D, Lichtner A, Jauffres D et al (2015) Effective transport properties of 3D multi-component microstructures with interface resistance. Comput Mater Sci 96:277–283. https://doi.org/10.1016/j.commatsci.2014.09.027
28. Renouf M, Fillot N (2008) Coupling electrical and mechanical effects in discrete element simulations. Int J Numer Methods Eng 74:238–254. https://doi.org/10.1002/nme.2157
29. Bourbatache K, Guessasma M, Bellenger E et al (2012) Discrete modelling of electrical transfer in multi-contact systems. Granular Matter 14:1–10. https://doi.org/10.1007/s10035-011-0307-y
30. Zohdi T (2014) A direct particle-based computational framework for electrically enhanced thermo-mechanical sintering of powdered materials. Math Mech Solids 19:93–113. https://doi.org/10.1177/1081286513505472
31. Hubert C, André D, Dubar L et al (2017) Simulation of continuum electrical conduction and Joule heating using DEM domains. Int J Numer Methods Eng 110:862–877. https://doi.org/10.1002/NME.5435
32. Becker V, Birkholz O, Gan Y et al (2021) Modeling the influence of particle shape on mechanical compression and effective transport properties in granular lithium-ion battery electrodes. Energy Technol 9:886. https://doi.org/10.1002/ente.202000886
33. Zhu Y, Dong E, Wang Y et al (2021) Research on the variation of resistance of granular system with different sizes under compressive stress. J Appl Phys 129:032606. https://doi.org/10.1063/5.0032606
34. Zeng C, Renouf M, Berthier Y et al (2016) Numerical investigation on the electrical transmission ability of a shearing powder layer. Granular Matter. https://doi.org/10.1007/s10035-016-0619-z
35. Coble R (1958) Initial sintering of alumina and hematite. J Am Ceram Soc 41:55–62. https://doi.org/10.1111/j.1151-2916.1958.tb13519.x
36. Rojek J, Kasztelan R, Tharmaraj R (2022) Discrete element thermal conductance model for sintered particles. Powder Technol 405:117521. https://doi.org/10.1016/j.powtec.2022.117521
37. Nisar F, Rojek J, Nosewicz S et al (2024) Evaluation of effective thermal conductivity of sintered porous materials using an improved discrete element model. Powder Technol 437:119546. https://doi.org/10.1016/j.powtec.2024.119546
38. Stoer J, Bulirsch R (1992) Introduction to numerical analysis, 2nd edn. Springer, Berlin
39. Balod A, Sarraf ZA, Basheer E (2020) Comparison between dynamic discrete element method and static discrete element method to determine neck size between powders during sintering process. J Eng Sci Technol Rev 13(6):159–165. https://doi.org/10.25103/jestr.136.22
40. Wonisch A, Kraft T, Moseler M, Riedel H (2009) Effect of different particle size distributions on solid-state sintering: a microscopic simulation approach. J Am Ceram Soc 92:1428–1434. https://doi.org/10.1111/j.1551-2916.2009.03012.x
41. Martin C, Yan Z, Jauffres D et al (2016) Sintered ceramics with controlled microstructures: numerical investigations with the discrete element method. J Ceram Soc Jpn 124(4):340–345. https://doi.org/10.2109/jcersj2.15269
42. Nosewicz S, Rojek J, Pietrzak K et al (2013) Viscoelastic discrete element model of powder sintering. Powder Technol 246:157–168. https://doi.org/10.1016/j.powtec.2013.05.020
43. Nosewicz S, Rojek J, Chmielewski M et al (2017) Discrete element modeling and experimental investigation of hot pressing of intermetallic nial powder. Adv Powder Technol 28:1745–1759. https://doi.org/10.1016/j.apt.2017.04.012
44. Nosewicz S, Jurczak G, Chrominski W et al (2022) Combined EBSD and computer-assisted quantitative analysis of the impact of spark plasma sintering parameters on the structure of porous materials. Metall Mater Trans A 53:4101–4125. https://doi.org/10.1007/s11661-022-06821-z
45. Kincaid D, Cheney W (1991) numerical analysis. Mathematics of scientific computing. Brooks/Cole Publishing, Salt Lake City